Sensors and Actuators A 159 (2010) 41–50

Contents lists available at ScienceDirect

Sensors and Actuators A: Physical

journal homepage: www.elsevier.com/locate/sna

Latching in a MEMS shock sensor: Modeling and experiments

Luke J. Currano[a,b,*], Miao Yu[b], Balakumar Balachandran[b]

[a] U.S. Army Research Laboratory, 2800 Powder Mill Rd, Adelphi, MD 21046, United States
[b] Department of Mechanical Engineering, University of Maryland, College Park, MD 20742, United States

ARTICLE INFO

Article history:
Received 20 October 2009
Received in revised form 25 January 2010
Accepted 11 February 2010
Available online 18 February 2010

Keywords:
Shock sensor
Acceleration switch
Threshold
Latching
Reduced-order model
Inertial switch

ABSTRACT

Modeling, numerical, and experimental efforts undertaken to develop a fundamental understanding of latching in a MEMS shock sensor are presented. A two degree-of-freedom model is developed and numerical studies are conducted with this model. These studies, which help shed light on difficult to observe experimental aspects, are used to examine the interaction forces between the shock sensor mass and latch, bounce effects, and loss of contact between the mass and the latch. High-speed video images of the shock sensor motions collected during a latching event are shown, and these results are used to verify the model predictions. Parametric studies conducted to examine the sensitivity of the design to friction and the effects of the latch mass and stiffness properties on the latch bounce are presented and discussed.
Published by Elsevier B.V.

1. Introduction

Impact is a critical damage-inducing mechanism in microelectronics. Monitoring the acceleration of a system can provide valuable information about the severity of an impact event and the likelihood of damage due to this event. Standard accelerometers impose a constant parasitic power draw even when no acceleration or impact is present. Furthermore, in small-scale and/or long-lifetime systems where the power supply is limited, the accelerometer power draw can significantly reduce the useful monitoring period before the power source has to be changed or recharged. An acceleration sensor that requires no power to monitor acceleration is therefore attractive in many health monitoring applications.

Various types of acceleration switches have been proposed to provide no-power monitoring of acceleration [1–11]. These devices are triggered at a given acceleration threshold, and a circuit is either closed or opened in response to an acceleration level above this threshold. While this measurement of maximum acceleration does not give sufficient information to conclude whether or not damage has occurred [12], it can alert the user to the fact that a potentially damaging event has occurred and an inspection of the system is required.

Acceleration switches can be broadly classified into intermittent [1–3] and persistent types [4–8], depending on whether the switch remains in a changed state after the end of an acceleration pulse. The persistent type devices can be further classified depending on the mechanism which holds the sensor in the switched state. This classification includes the following: (i) bistable mechanism based switches [4–6], (ii) electrostatic latching switches 0 and (iii) physically latching switches [8–11]. Physically latching switches include some form of mechanical lock, which prevents the switch from returning to the unperturbed position. Typically, this involves a latch that is compliant in the direction perpendicular to the direction of sensor travel and stiff in the direction parallel to the travel direction. Curved or angled surfaces are used to redirect the contact forces along the normal (compliant) direction while the sensor is moving past the latch, and flat surfaces ensure that all of the contact force during relaxation is directed along the travel (stiff) direction. In prior work on physically latching MEMS acceleration switches, only simple (often static) models have been considered and the characterization results have been limited to the accelerations required to latch the devices.

The design explored in this paper is a physically latching switch design, as shown in Fig. 1. The sensor consists of a large proof mass suspended by four springs, and four cantilevered latches (two for sensing acceleration in the positive direction and two for the negative direction). The latches have quarter-round interface surfaces, as do the corresponding contact points on the mass. When subjected to an acceleration directed along the *Y*-axis, the system moves away from its resting state. The springs deform to accommodate the motion of the mass and also impart a restoring force

* Corresponding author at: U.S. Army Research Laboratory, RDRL-SER-L, 2800 Powder Mill Rd, Adelphi, MD 20783, United States. Tel.: +1 301 394 0566.
E-mail address: luke.currano@us.army.mil (L.J. Currano).

0924-4247/$ – see front matter. Published by Elsevier B.V.
doi:10.1016/j.sna.2010.02.008

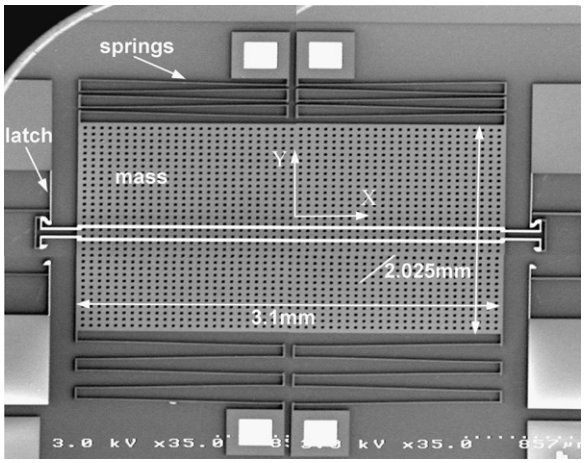

Fig. 1. SEM of latching shock sensor design (composite of four images due to large overall size of sensor).

that acts to move the mass back to the resting state. If the acceleration is large enough, the mass will eventually contact the latches. The interaction of the mass with the latches is illustrated in Fig. 2. During contact, the curved surfaces of the latch and the contact surfaces on the mass redirect the contact force along the contact normal. Hence, a portion of the contact force goes into bending of the cantilever beam (Fig. 2ii). If the acceleration is high enough that the mass continues to move, the mass eventually pushes all the way past the latch, the contact force drops to zero, and the latch springs back to its equilibrium position (Fig. 2iii). If the acceleration magnitude is large enough, the mass continues to move and loses contact with the back surface of the latch (Fig. 2iv). When the acceleration is removed, the flat back surfaces of the quarter-round pieces come into contact. This prevents the mass from moving back to its resting state, and also closes the electrical circuit between the two latches. This is the desired electrical sensing mechanism for the sensor.

The fabrication, initial characterization, and a basic single degree-of-freedom (DOF) model for the latching sensor design of the authors have been presented in earlier work 0. The single DOF model is convenient to solve. However, in this model, it is assumed that the latch position depends on the position of the mass, and therefore, little insight is gained into the dynamics of the interaction of the mass and latch. In this article, the authors develop a two DOF model to provide an extended framework for study of the behavior of the latch and its interaction with the mass. The model results are compared with those obtained from the single DOF model 0. Interaction forces between the mass and latch and a "bounce" effect predicted by the new model are reported. In addition, high-speed video images of the latching event obtained for the first time in such a class of devices are presented. The model predictions are seen to be in good agreement with the motion characteristics observed in these images. Finally, the reduced-order model is used to carry out parametric studies to aid the design process.

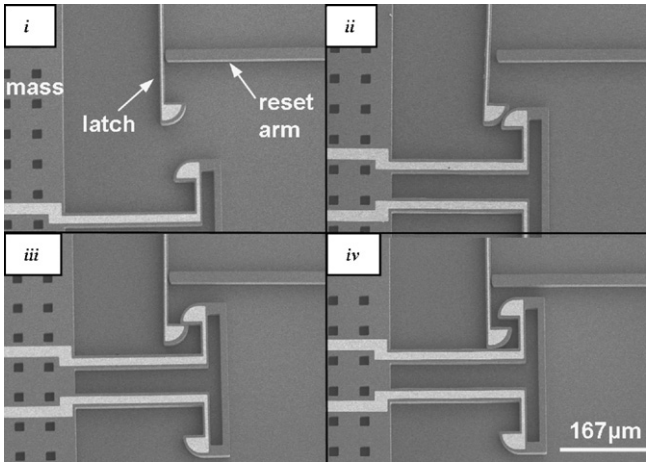

Fig. 2. Sequence of events during sensor latching: (i) before mass contacts latch, (ii) during contact, mass is sliding past latch, (iii) still in contact, mass has just moved past latch, and (iv) after contact, when mass has moved past latch for large acceleration magnitude.

2. Shock test experiments

The shock sensor was fabricated and studied on a shock table to gain insights into the sensor operation and experimentally verify the model predictions. The experimental arrangement is shown in Fig. 3. The acceleration applied to the shock sensor was monitored with a commercial accelerometer threaded directly into the shock table. The shock sensor was wire bonded to a dual inline package for electrical monitoring of the sensor and electrical reset in between experiments. For electrical monitoring, a voltage divider circuit was constructed. One latch of the sensor was connected to a DC power supply set to output 5 V, and the other latch was connected to a 1 MΩ resistor. The opposite end of the resistor is connected to ground. When the sensor latches, the circuit is closed and a voltage signal is detected across the 1 MΩ resistor. A computer with a data acquisition system was used to power the accelerometer and capture the acceleration data and the sensor output voltage.

A high-speed video camera was mounted on a microscope suspended over the shock table to visually capture the operations of the sensors. A 5× objective and 10× multiplier (for a total 50× magnification) were used to image the sensors. The accelerometer output was used to trigger an oscilloscope which in turn was used to trigger the high-speed camera. The accelerometer output, the trigger signal, and the frame synchronization output from the high-speed camera were all captured by using the oscilloscope. Since the oscilloscope had only had three channels, the voltage divider signal could not be captured with this oscilloscope. However, by matching the accelerometer trace from the data acquisition system and the oscilloscope, the trigger and frame synchronization could be synchronized with the voltage divider signal.

The individual frames from the high-speed video were analyzed by using a MATLAB routine (Fig. 4). With this routine, the image file is read into an array and resized to include only relevant parts of the frame based on user input, and the image brightness values (ranging from 0 to 255) are summed over each column. The gold traces on the mass are significantly brighter than the background, and these traces are easy to distinguish when the column sum is plotted. Since the background brightness varies with position (it is brightest in the center of the frame) and the sensor moves through the frame during the latch event, a global maximum does not necessarily suffice. Instead the frame is searched for a pair of local maxima corresponding to the two parallel gold traces across the mass. Similarly, the position of the chip can be tracked by assuming that there is no significant deflection of the second (inactive) latch in the direction parallel to the sensor axis. Here, an inactive latch refers to the latch for negative deflection when the direction of the applied acceleration makes the mass travel in the positive direction. Since the mass never contacts this latch and the ratio of stiffness to mass is very high, the assumption of no deflection is expected to be valid. Another local maximum can be found, and this maximum corresponds to the gold coating on top of the latch. By subtracting the motion of this local maximum (and therefore the motion of the shock table under the camera) from the motion of the mass, the rel-

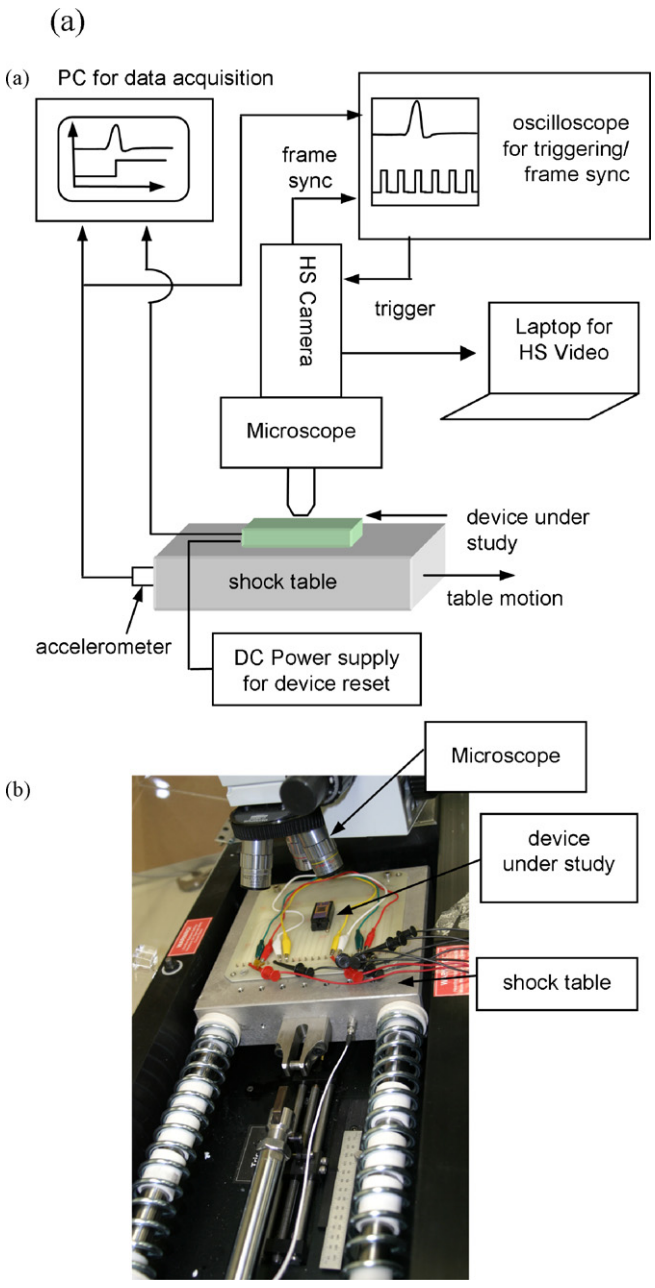

Fig. 3. Shock table experimental arrangement for high-speed video capture: (a) schematic of entire experimental system and (b) a photograph of shock table with device mounted under microscope.

ative motion of the mass with respect to the translating reference frame of the chip can be found. This relative motion is tracked by the model and this motion can be used to determine whether the sensor latches or not. When the relative motion exceeds 150 μm, it means that the mass has moved completely past the latch and it will remain latched until the sensor is reset.

3. Model and displacement responses

The authors extend their previous lumped parameter model 0 from one to two degrees of freedom, which eliminates the assumption of constant contact between the mass and latch and allows for study of the contact dynamics of the latch movement. The considered system consists of two latches and one mass, but due to symmetry only one latch is considered in the model. The mass is

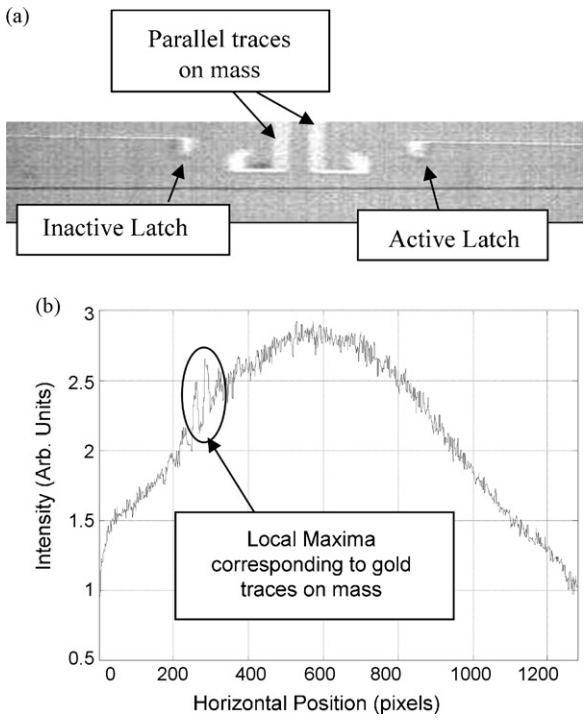

Fig. 4. Analysis of high-speed video frame: (a) image frame from high-speed video showing parallel traces and (b) analysis of image with two adjacent local maxima indicating mass position.

modeled with one degree-of-freedom, along the *Y*-axis, and the latch is modeled with one degree-of-freedom along the *X*-axis (see Fig. 5). The Lagrangian for the system can be written as

$$L = \frac{1}{2}M(\dot{y}_c + \dot{y}_{m/c})^2 + 2\left(\frac{1}{2}m\dot{x}^2\right) - \frac{1}{2}ky_{m/c}^2 - 2\left(\frac{1}{2}k_L x^2\right) - 2\left(\frac{1}{2}k_c\delta^2\right). \quad (1)$$

where M and m are the effective sensor mass and the effective latch mass, respectively; y_c represents the displacement of the chip on which the sensor is mounted, the chip motion serves as the forcing function for the system; $y_{m/c}$ represents the displacement of the

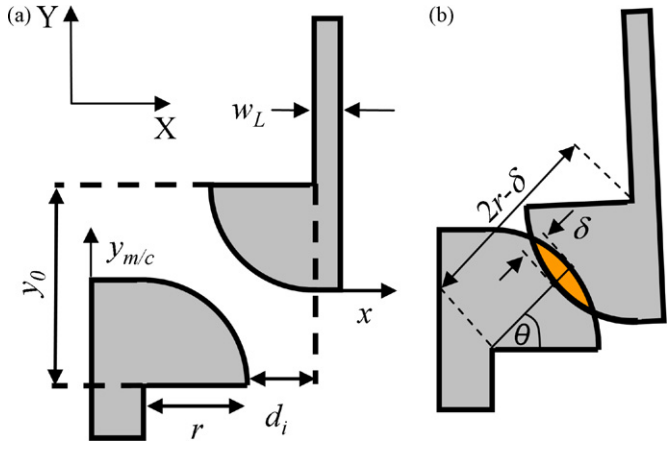

Fig. 5. Geometry of mass–latch interaction: (a) in resting position and (b) after contact. *X* and *Y* denote the coordinate axes for the reference frame. y_0, r, d_i, and w_L are design parameters corresponding to the travel before latching, the radius of the contact surfaces, the initial horizontal offset between contact surfaces, and the width of the latch cantilever, respectively. x and $y_{m/c}$ denote the degrees of freedom of the latch and the mass, respectively. θ is the angle of the contact normal with respect to the coordinate axes, and δ is the total contact deformation.

mass with respect to the chip (the first DOF); x denotes the displacement of the latch (the second DOF); and δ denotes the contact deformation of the mass and the latch, as illustrated in Fig. 5 (from which the coupling terms arise). The stiffness terms k, k_L, and k_c correspond to the effective spring constants of the sensor, the latch, and the contact, respectively.

The contact deformation is defined as being greater than or equal to zero. It is assumed that there is no adhesive or tensile contact force component. Given the positions of both the mass and the latch, the total contact deformation is prescribed by the need to avoid penetration of one body into another. The contact deformation can therefore be defined geometrically by inspection of Fig. 5b as a piecewise function of the position variables, x and $y_{m/c}$,

$$\delta = \begin{cases} 2r - \sqrt{(y_0 - y_{m/c})^2 + (r + d_i + x)^2}, & \sqrt{(y_0 - y_{m/c})^2 + (r + d_i + x)^2} \le 2r \\ 0, & \sqrt{(y_0 - y_{m/c})^2 + (r + d_i + x)^2} > 2r \end{cases}, \tag{2}$$

where y_0, r, and d_i are design parameters denoting the required travel of the mass from the resting state to the latched state, the radius of the contacting surfaces, and the initial offset of the two contacting surfaces, respectively, as shown in Fig. 5.

The contact force is approximated as a linear spring force. The spring constant is based on a force–deflection relationship derived from Hertzian contact theory by Puttock and Thwaite [13]. Their treatment is meant for two identical cylinders in contact, and allows for an arbitrary cylinder length. In Hertzian contact theory, the following assumptions are made: (i) the contact surfaces are completely smooth, (ii) the bodies are isotropic and linearly elastic, (iii) the elastic limits are not exceeded, and (iv) there are no friction forces in action. While these assumptions do not hold true for the silicon contact surfaces (the surfaces have roughness on the order of 60 nm, silicon has moderately anisotropic modulus and the sliding contact must necessarily include friction), simplifications are needed to derive a closed-form solution for the contact force–deformation relationship. According to Puttock and Thwaite, in general, the friction forces and varying elastic moduli lead to deviations of less than 10% from the ideal cases that they had studied. On this basis, for two identical cylinders in contact, the force–deflection relationship can be approximated as 0

$$\delta = 2PB\left[1 + \ln\left(\frac{a^2}{PBr}\right)\right], \tag{3}$$

where P is the force per unit length pressing the cylinders together, r is the cylinder radius, a is the length of contact region, and B is a material property parameter defined as

$$B = \left(\frac{1 - \upsilon^2}{\pi E}\right), \tag{4}$$

where E is the Young's modulus and ν is the Poisson's ratio of the material. To obtain a linear spring constant from (3), the authors solve for the deflection at the maximum expected contact force and obtain the ratio of the force to deflection.

The equations of motion governing the sensor can be derived from the Lagrange equations, and they are of the form

$$M(\ddot{y}_c + \ddot{y}_{m/c}) + k y_{m/c} + 2k_c\delta\frac{\partial\delta}{\partial y_{m/c}} = -sgn(\dot{y})2\mu k_c\delta\cos\theta, \tag{5}$$

$$m\ddot{x} + k_L x + k_c\delta\frac{\partial\delta}{\partial x} = -sgn(\dot{x})\mu k_c\delta\sin\theta, \tag{6}$$

where μ is the coefficient of friction and θ is the contact angle, given by:

$$\theta = \arcsin\left(\frac{y_0 - y_{m/c}}{2r - \delta}\right). \tag{7}$$

The partial derivatives of δ can be obtained as

$$\frac{\partial\delta}{\partial y_{m/c}} = \frac{(y_0 - y_{m/c})}{\sqrt{(y_0 - y_{m/c})^2 + (r + d_i + x)^2}}, \tag{8}$$

$$\frac{\partial\delta}{\partial x} = -\frac{(r + d_i + x)}{\sqrt{(y_0 - y_{m/c})^2 + (r + d_i + x)^2}}, \tag{9}$$

which can be substituted into (5) and (6). The solutions of these equations can be numerically determined for any set of chosen initial conditions and any given external acceleration profile to which the chip is subjected. The chip acceleration serves as an excitation to the system. Although the model can accommodate any arbitrary function for the chip displacement y_c, in this article, this forcing profile is considered to be a half-sine pulse for all simulations with the magnitude and duration of the half-sine pulse as noted in each case. To carry out the simulations, it is assumed that the chip is at rest prior to the onset of the imposed acceleration and the initial conditions are zero; that is $(x, \dot{x}, y_{m/c}, \dot{y}_{m/c}) = (0.0, 0.0, 0.0, 0.0)$ at $t = 0$). The solutions to (5) and (6) were obtained by using the Matlab differential equation solver ODE45, which is based on an explicit Runga–Kutta (4, 5) scheme. The time step settings were systematically varied until there was no further effect on the results and convergence was observed. The authors found that an initial time step of 0.5 ns and a maximum time step of 100 ns were necessary to accurately capture the onset of contact.

The relevant parameters for the two sensor designs considered here are shown in Table 1. The results obtained from a representative simulation conducted for one sensor design and the acceleration profile are shown in Fig. 6. The latch initially does not undergo any motion because the mass has not contacted it. Contact is made at 1.1 ms in this case. At 1.4 ms, the mass has moved completely past the latch. After this event, in the simulations, the motions of the shock sensor mass and latch are treated as uncoupled. The latch undergoes free vibrations at the natural frequency of the latch (44.7 kHz), while the mass bounces back and forth as it alternately contacts the extension frame and flat edge of the latch (see Fig. 7). The bouncing of the mass in this case has a frequency of

Table 1
Design parameters for shock sensor. The term "uncoupled" is used here to denote parameters that cannot be readily defined for the system, but can be defined for either the mass or latch independent of the system.

Parameter	Description	Design 1	Design 2
H_m (mm)	Height of mass	2.025	2.025
W_m (mm)	Width of mass	4.0	3.1
M (kg)	Sensor mass	3.42e-7	2.65e-7
L_f (mm)	Length of suspension spring	1.945	1495
W_f (mm)	Width of suspension spring	12	12
k (N/m)	Suspension spring stiffness	0.601	1.324
f (Hz)	Natural frequency of sensor (uncoupled)	211	356
w_L (μm)	Width of latch cantilever	8	8
l_L (μm)	Length of latch cantilever	460	460
r (μm)	Latch radius	40	40
d_i (μm)	Horizontal offset	15	15
m (kg)	Latch effective mass	5.64e-11	5.64e-11
k_L (N/m)	Latch stiffness	4.44	4.44
f_L (Hz)	Natural frequency of latch (uncoupled)	44,700	44,700
k_c (N/m)	Contact stiffness	5.57e5	5.57e5
y_0 (μm)	Initial sensor travel to latch	150	150
$\ddot{y}_{crit}$ (g)	Nominal threshold acceleration for latching	50	100

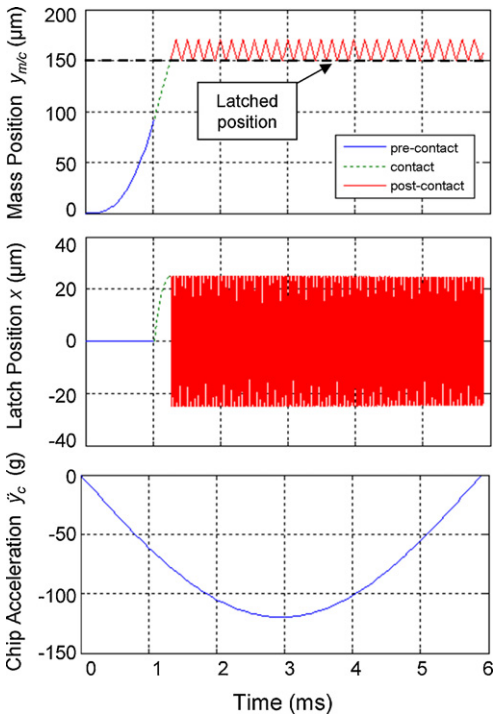

Fig. 6. Design 2 sensor results obtained from two DOF model for position of mass ($y_{m/c}$) and position of latch (x) when $\mu = 0.1$, and acceleration pulse is 120 gs for 5.9 ms.

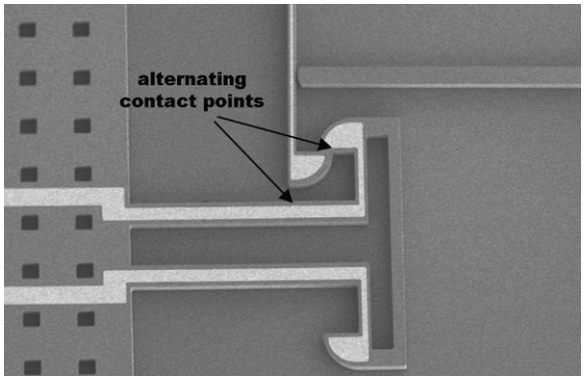

Fig. 7. Image of latched sensor illustrating alternating contact locations, after latching.

around 4.0 kHz. The time intervals associated with the mass bouncing back and forth after latching is primarily dependent on the speed of the mass after latching, which dictates the time windows between impacts with the extension frame, but there is also a secondary dependence on the mass and spring constant of the sensor as well. The motion of the latch in the post-contact region is treated as a free harmonic oscillation with an initial displacement equal to the position of the latch when the mass has just moved past it. As shown in Fig. 6, the frequency of vibration of the latch (44.7 kHz) is much higher in this post-contact region than that of the mass bounce frequency (4.0 kHz). This is due to the much lower mass and higher spring constant of the latch.

4. Contact force and interpenetration results

The force–deflection relationship used in the model was also compared with the relationship determined through a three-dimensional finite element analysis by using ANSYS (Fig. 8). Half-cylinders were used to allow application of a uniformly

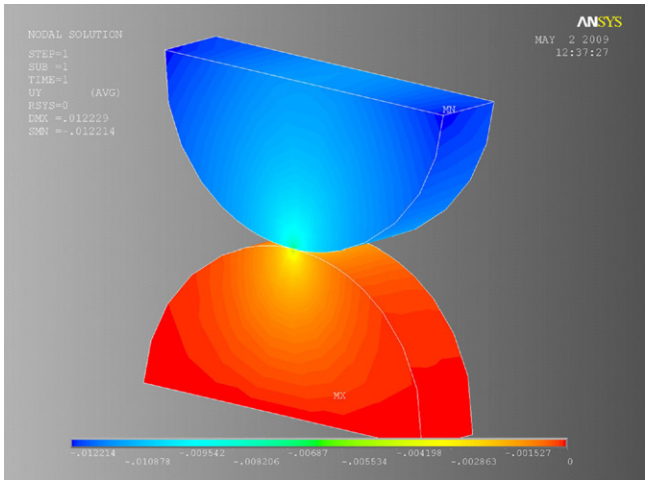

Fig. 8. Finite element model of latch contact.

distributed force normal to a flat edge. Eighty-eight thousand tetrahedral Solid95 elements (a structural element with mid-side nodes) were used to conduct a static analysis of the contact subjected to a constant applied force. Each node of the Solid95 element has three displacement degrees of freedom. The flat edge of one half-cylinder was fully constrained, while the load is applied to the flat edge of the other half-cylinder. The contact mode used was surface-to-surface, flexible/flexible, with the 3D contact surface elements being Targe170 and Conta174. Default settings for the contact elements were used, including a penalty stiffness factor of 1.0 and a penetration tolerance factor of 0.1. The loads chosen are in the range of the expected contact forces predicted by the dynamic shock sensor model discussed in the previous section. The deflection of the edge where the load was applied is equal to the contact deformation used in the model. The finite element results are compared with the results obtained from (3) in Fig. 9. The linear approximation used in the model is also included in the plot. The linear approximation has to pass through (0, 0) for consistency, so that the contact force is zero when the contact deformation δ is zero. The other point for the linear approximation was taken from (3), when the contact force is 5 mN, based on the maximum contact force encountered over a range of representative simulations.

The contact force can be extracted from the model at each time step to help analyze the behavior. The results obtained for a Design 2 sensor device are shown in Fig. 10. The dynamics of the contact interaction result in the oscillatory character of the contact force.

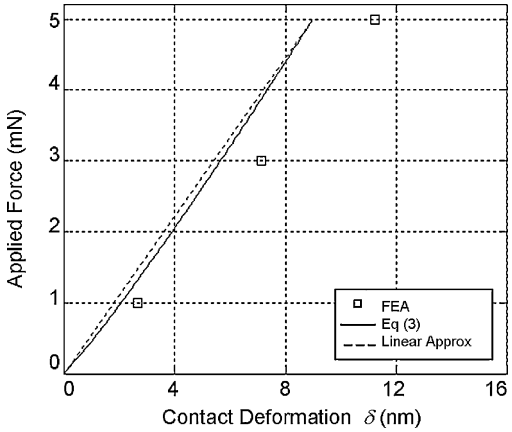

Fig. 9. Comparison of contact force-deflection relationship predicted by Eq. (3) with finite element results.

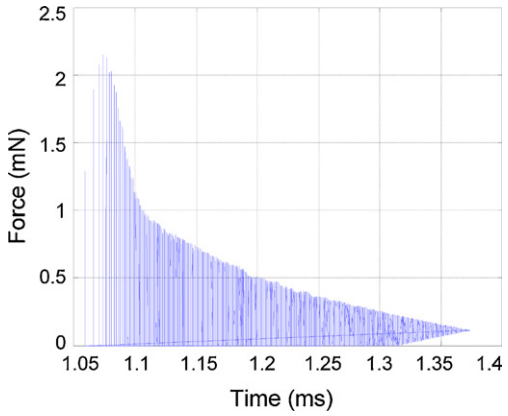

Fig. 10. Predicted time history of contact normal force for Design 2 sensor when $\mu = 0.1$ and acceleration pulse is 120 gs for 5.9 ms.

Specifically, the sudden onset of contact with high relative speed is similar in action to that of a step forcing function. The finite stiffness of the latch and the contact result in vibration of the latch and alternating deformation/relaxation of the contact region. As the mass pushes past the latch, the direction of the contact normal changes from just over 45° from the direction of travel at the moment of first contact to 90° to the direction of travel just before latching. This results in a steady decline in the magnitude of the resisting force from the latch, which explains the steady decrease in the amplitudes of the contact force oscillations. The force does not decline to zero at the end of the contact phase since the spring force of the latch acts on the contact even though the contact normal is essentially perpendicular to the direction of travel of the mass. At the point just before latching, the mass causes the latch to displace by at least $(r - d_i)$.

Early on in the contact phase, the prediction of the model is that there is intermittent contact due to latch bounce directed away from the mass. This is evident in Fig. 11, in which the position of the latch is shown during the first few microseconds of contact (this is an expanded view of the contact section of the latch position graph from Fig. 6). There is a clear bounce generated by the contact force pushing the latch away from the mass. The time steps need to be carefully chosen in order to capture the bounce motions. In the present case, as the time step is decreased towards zero, the magnitude of the bounce approaches a limit of about 0.5 μm. For the Design 2 sensor, the initial bounce causes a loss of contact for 7.0 μs. This corresponds to an initial bounce oscillation at about 140.0 kHz, which is much higher than the uncoupled natural frequency of either the mass or latch. This is because the bounce frequency is dependent on the stiffness and mass of the latch, the contact stiffness and deformation of the contact, and the position and speed of the sensor mass. Specifically, since the position of the mass prevents the latch from undergoing full free-vibration cycles, the bounce frequency can be much higher than that of the free-vibration frequency of the latch. After the first bounce, each successive bounce gets smaller in magnitude and the loss of contact duration shorter until after about 300 μs, when there is no longer any loss of contact. This corresponds to a time of about 1.3 ms in Fig. 10, when the oscillations in the contact force no longer drop to zero between cycles.

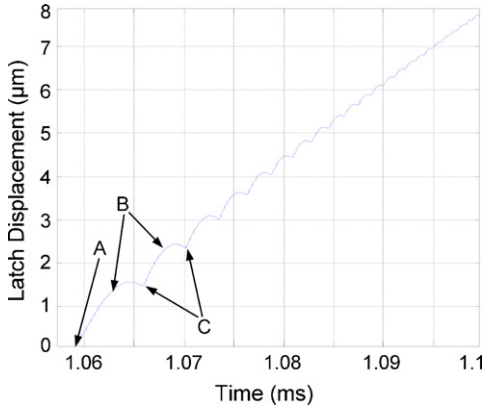

Fig. 11. Position of latch during initial phase of contact, displaying bounce of up to 0.4 μm (expanded view of the contact section in the latch position graph from Fig. 6). Point A is where initial contact is made, points B are where contact is lost during a bounce, and points C are where contact is reestablished after a bounce.

5. Comparisons between single DOF and two DOF model results

To compare the results obtained between the two DOF model from the current work and the single DOF model of prior work [10], the displacement time histories are plotted for one case in Fig. 12. The difference between the two models is in the treatment of the contact force between the latch and the mass. In the single DOF model, the displacement of the mass is used to calculate the position of the latch (assuming contact is maintained). The position of the latch and the resultant spring force are subsequently used to calculate the normal force acting on the mass. In the two DOF model, a position for the latch is not assumed, and the contact force is calculated based on the relative positions of the mass and latch by using the contact stiffness derived from Hertzian contact theory. The results obtained from the two models are identical before contact is made, as expected. During contact, the results differ. The coefficient of friction affects the mass motion more strongly in the single DOF model since the latch and mass are in constant contact, whereas in the two DOF model the latch bounces away from the mass many times during the nominal contact period. This is evident when the contact forces are compared (Fig. 13). Although the magnitude of the contact force in the single DOF model is only about 10% of the maximum magnitude of the contact force determined in the two DOF model, the work done by the friction force is higher in the case of the single DOF model because the distance travelled during contact is much larger.

The increased dissipation in the single DOF model is due to the larger work done by the friction force, which leads to a lower speed of the mass after latching. The predicted frequency of the oscil-

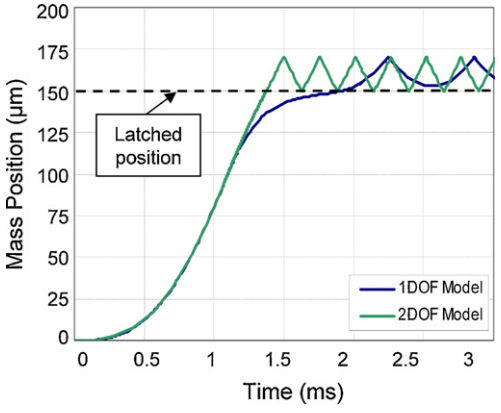

Fig. 12. Design 2 sensor: comparisons of single DOF model results [10] to DOF model results when $\mu = 0.1$ and acceleration pulse is 120 gs for 5.9 ms.

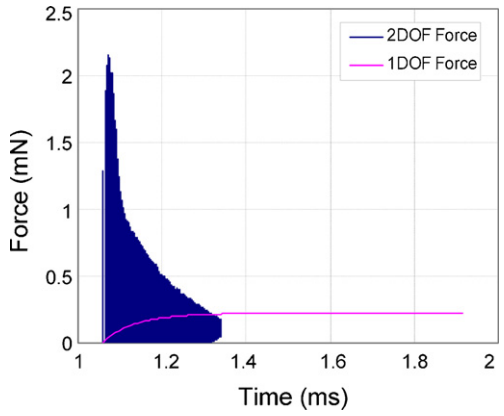

Fig. 13. Comparison of normal forces determined from single DOF and two DOF models.

lations after latching is therefore also lower with the single DOF model than with the two DOF model.

6. High-speed video images and comparisons

To validate the proposed model, two different sensors were tested and filmed by using a high-speed camera. The two sensors corresponded to two different design threshold levels, as given in Table 1: (i) Design 1 sensor with a nominal 50 gs (50 times gravitational acceleration) threshold and (ii) Design 2 sensor with a nominal 100 gs threshold. The only differences between the two designs are in the lengths of the springs and the size of the mass. The widths of the springs, the sizes and stiffness properties of the latches, and the travel required to latch are all identical. The video images were captured at 4261 frames per second, which is the maximum camera frame rate possible with a reasonable pixel resolution.

The various frames obtained from one high-speed video capture for the Design 1 sensor are shown in Fig. 14 along with line drawings of the latch positions generated by using the two DOF model at the same time instants. The time steps, which are shown on the line drawings, correspond to the frame rate of the high-speed video capture. An examination of the line drawings and the high-speed video frames shows a very good qualitative agreement between the two, including an identical number of frames when the mass is in contact with the latch (frames 9–11), before moving past it.

For a quantitative measure of the model performance, the model results are also compared with the relative mass motion information extracted from the high-speed video images. The comparisons are shown in Figs. 15 and 16 for the Design 1 sensor and the Design 2 sensor, respectively. A friction coefficient of $\mu = 0.1$ was used to make the model predictions. The results obtained for the Design 1 sensor match the high-speed video measurements very well. There are not as many data points from the high-speed video images for the Design 2 sensor, since the response is faster, and the match is not quite as good as that seen for the Design 1 sensor. However, the overall time to latch matches well and the predicted position before latching is fairly close to the high-speed video results, although the model prediction is outside the error bars for the third and fourth frames. Altogether, the comparisons confirm that the constructed reduced-order model predicts the device performance well.

Regarding the loss of contact, or bounce of the latch predicted by the model, there is no confirmation of this in the high-speed video images because the magnitude and duration of the bounces are too small to be captured (0.5 μm and 7.0 μs respectively for the Design 1 sensor). The video resolution is about 2.5 μm/pixel and the time interval between frames is 0.23 ms, both of which are too

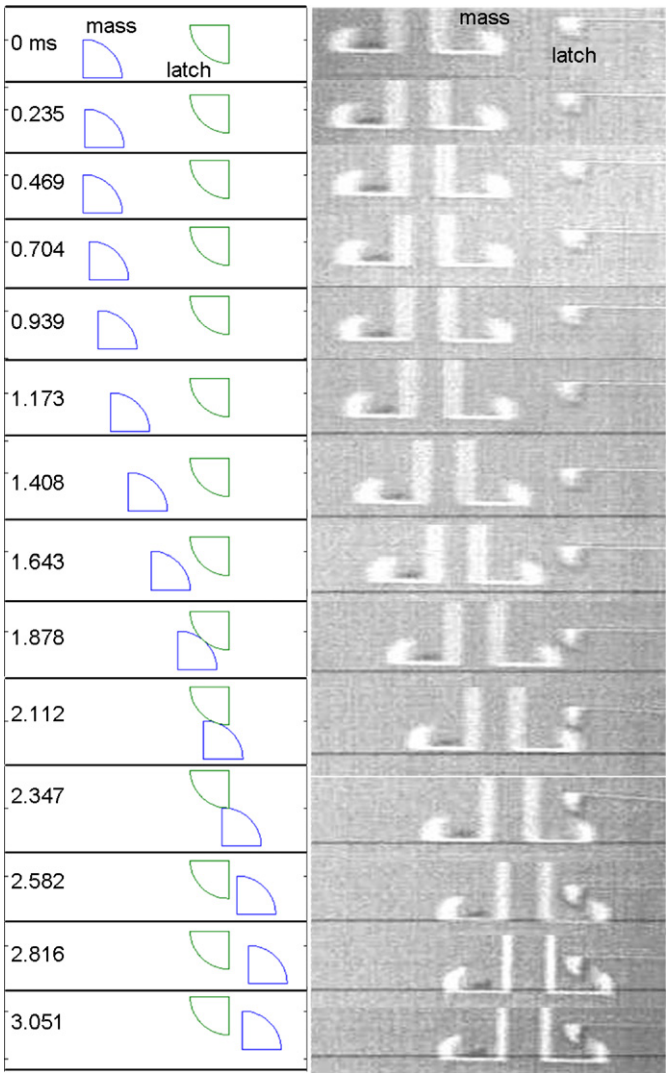

Fig. 14. Design 1 sensor: comparisons of model predictions with high-speed video frame results.

large to see any bouncing motions that might be occurring. It may be possible to confirm this electrically in future work. However the current device is designed to close the electrical circuit only after the sensor latches. This was intended to distinguish near-latch events from fully latched events, and this was accomplished by coating only the flat side of the latches with a contact metallization layer. Future design iteration will include contact metallization of the rounded latch surface in addition to the flat latch surface in order to electrically verify the bounce effect.

7. Parametric studies

To generate information that could be useful for design of similar sensors, the two DOF model has been used to study the effect of various parameters on the device performance. The authors began by examining the design variables that can be used to design devices to latch at various acceleration thresholds. As there are a large number of geometric parameters that can be changed, an exhaustive study is beyond the scope of this article. For instance, the sensor mass M can be changed by modifying the length or width of the mass, or changing the size or spacing of the etch holes. The stiffness of the sensor k can be changed by modifying the length or width of the springs, the number of meanders, or the number of suspension springs used. However, by focusing on one parameter that affects

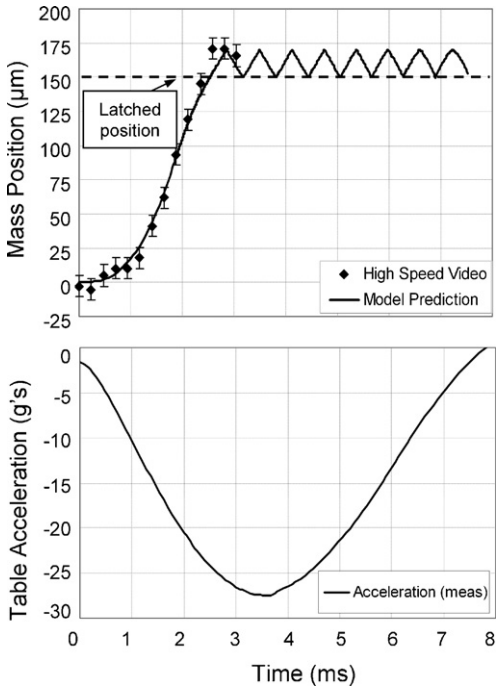

Fig. 15. Comparison of model predictions with high-speed video measurements for Design 1 sensor. The measured acceleration profile of the shock table is also plotted.

the stiffness and one that affects the mass of the sensor, a series of designs can be generated covering a wide range of acceleration thresholds. The geometric parameter used to change the sensor mass M for this study was the height of the mass H_m. The acceleration to latch as a function of H_m is shown in Fig. 17. The sensor mass (shown at the top of the plot) scales nearly linearly with the height of the mass; a slight nonlinear characteristic is seen for small values of H_m since the equivalent mass of the springs has a larger

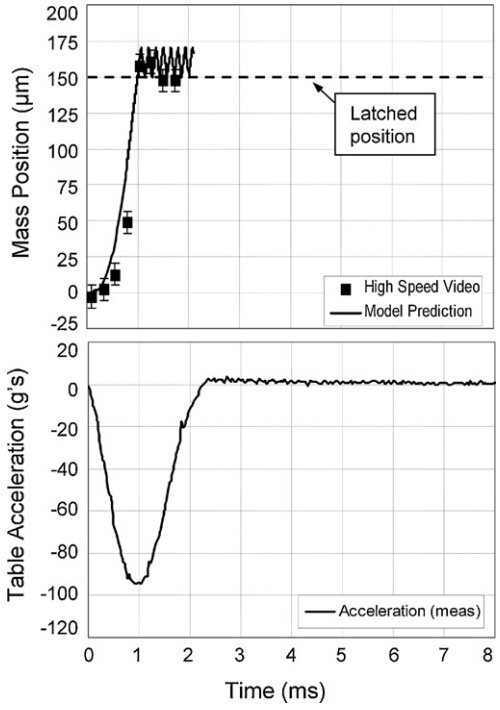

Fig. 16. Comparison of model predictions with high-speed video measurements for Design 2 sensor.

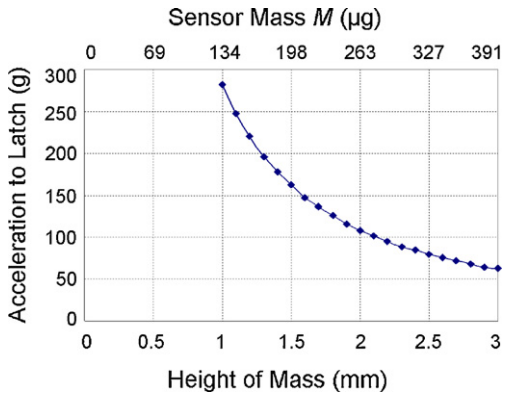

Fig. 17. Effect of vertical mass dimension on acceleration to latch. All other parameters are as the same as that previously used for Design 2 sensor.

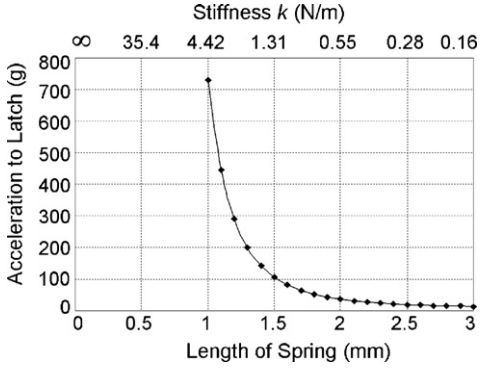

Fig. 18. Effect of suspension spring length on acceleration to latch. All other parameters are the same as that previously used for Design 2 sensor.

effect on the overall mass. As H_m (and the sensor mass) increases, the acceleration to latch decreases. The geometric parameter used to change the stiffness k for this study was the length of a spring. This has a more dramatic effect on the acceleration to latch for two reasons: (i) the stiffness scales with the inverse of the cube of the length and (ii) the width of the mass is tied to the length of the springs in the model, causing the mass to also decrease as the stiffness increases. The variation in acceleration to latch with respect to the spring length is shown in Fig. 18.

The characteristics of the latch also have an influence on the acceleration to latch. Since the coefficient of friction can vary somewhat due to the fabrication process and over a number of cycles [14,15], the acceleration required to latch the device is plotted over a range of friction coefficients in Fig. 19. The acceleration required

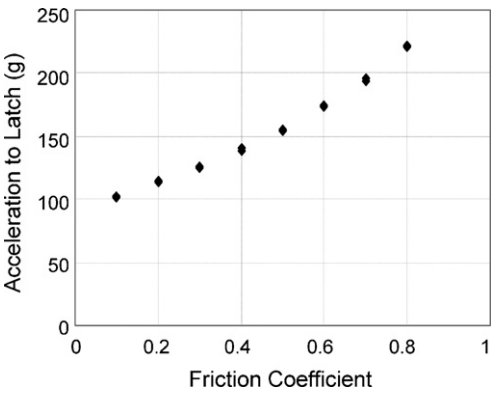

Fig. 19. Effect of friction coefficient on latching level for Design 2 sensor.

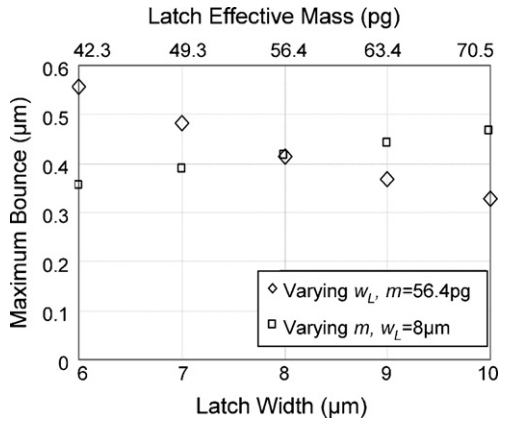

Fig. 20. Effects of varying latch width and effective latch mass on bounce magnitude for Design 2 sensor, when acceleration pulse is 140 gs for 5.9 ms.

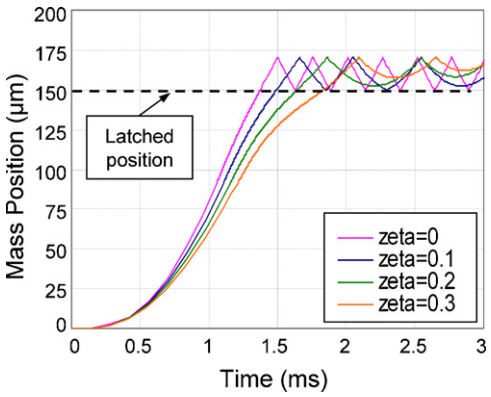

Fig. 21. Design 2 sensor responses for various damping factors zeta, when $\mu = 0.1$ and acceleration pulse is 120 gs for 5.9 ms. The undamped case (zeta = 0) corresponds to the results presented in Fig. 12.

to latch increases quickly with increase in the friction coefficient value. Good control over the fabrication process is therefore critical with this particular shock sensor design. In future work, optimization of the design will be explored to decrease the sensitivity to the friction coefficient.

The bounce of the latch is an important aspect to characterize device performance that has never been reported before for latching shock sensors. The two DOF model allows further study of the latch bounce phenomenon. The bounce dynamics are determined by the stiffness of the latch, the effective mass of the latch, and the speed of the mass when it hits the latch. In Fig. 20, the variation of the first bounce amplitude (which is also the amplitude for the largest bounce) is shown with respect to changes in the latch stiffness and latch mass. Here the latch stiffness was changed by varying the latch width. The effective mass was determined by making use of the latch dimensions, the density of silicon, and assuming vibration in the first cantilever mode. The mass of the latch was changed directly to match each of the total effective masses calculated by changing the latch width (equivalent to adding a point mass at the end of the latch). As the latch width is increased, the stiffness increases with the cube of the width and the mass increases linearly with the width. The result is that the bounce gets smaller as the width of the latch increases since the system inertia increases more slowly than the force keeping the latch in contact with the mass. When the mass of the latch is increased while keeping the latch stiffness constant, the system inertia increases and the force keeping the latch in contact with the mass remains the same, and this results in an increase of the bounce amplitude.

In the model presented in Section 3, the only dissipative force is due to the friction force that arises during the contact between the mass and latch. There may in fact be some damping effects due to air resistance and/or material damping due to stretching of the springs present throughout the entire sensor operation. This can be considered in the model by including a damping term in the equation of motion governing the sensor mass; that is, modifying Eq. (5), so that it reads as

$$M(\ddot{y}_c + \ddot{y}_{m/c}) + c\dot{y}_{m/c} + ky_{m/c} + 2k_c\delta\frac{\partial\delta}{\partial y_{m/c}} = -sgn(\dot{y})2\mu k_c\delta\cos\theta \tag{10}$$

where c is the damping constant for the mass. The effect of including this damping on the response of the mass is shown in Fig. 21. The damping constant c has been converted to the damping ratio zeta for ease of interpretation, where zeta = 0 corresponds to the undamped case and zeta = 1 corresponds to the critically damped case. As expected, the time to latch increases as the associated damping factor is increased, and the acceleration level required to latch also increases as the damping factor is increased. The bouncing of the mass after latching is also attenuated with inclusion of this damping. The oscillations after latching decrease in frequency with increased damping because the speed of the mass is decreased after latching.

8. Conclusions

A modeling and experimental framework for examining the latching dynamics of a latching MEMS shock sensor has been proposed in this paper. In the modeling component, a two degree-of-freedom reduced-order model is developed. The shock sensor mass and latch are treated as separate bodies, and a degree-of-freedom is associated with each of them. Coupling between the respective motions arises due to the contact force between them. The contact force is determined by using a linear contact stiffness derived from Hertzian contact theory. The model has been used to examine the dynamics of contact, and a latch bounce phenomenon is observed in the simulations.

In the experimental component of the work, a high-speed video camera mounted on a microscope over a shock table is used to image the shock sensor motions during the latching event. The position of the mass is tracked in each frame, and the results are compared with the predictions from the two DOF model. Good agreement is observed between the experimental results and model predictions. Envisioned future work includes use of the developed model for optimizing the shock sensor design, including determination of the minimal dimensions of the sensor for a given latching acceleration, and generation of robust designs that are relatively insensitive to small changes in the friction coefficient caused by process variations.

References

[1] Y. Loke, G.H. McKinnon, M.J. Brett, Fabrication and characterization of silicon micromachined threshold accelerometers, Sens. Actuators A 29 (1991) 235–240.
[2] Z. Yang, G. Ding, W. Chen, S. Fu, X. Sun, X. Zhao, Design, simulation and characterization of an inertia micro-switch fabricated by non-silicon surface micromachining, J. Micromech. Microeng. 17 (2007) 1598–1604.
[3] A. Selvakumar, N. Yazdi, K. Najafi, A wide-range micromachined threshold accelerometer array and interface circuit, J. Micromech. Microeng. 11 (2001) 118–125.
[4] B.J. Hansen, C.J. Carron, B.D. Jensen, A.R. Hawkins, S.M. Schultz, Plastic latching accelerometer based on bistable compliant mechanisms, Smart Mater. Struct. 16 (2007) 1967–1972.
[5] J.W. Wittwer, M.S. Baker, J.A. Mitchell, D.S. Epp, R.C. Clemens, M.R. Brake, J.A. Walraven, The Sandia MEMS passive shock sensor: FY08 design summary, Sandia National Laboratories Technical Report SAND2008-7203, 2008.

[6] M. Jia, X. Li, Z. Song, M. Bao, Y. Wang, H. Yang, Micro-cantilever shocking-acceleration switches with threshold adjusting and 'on'-state latching functions, J. Micromech. Microeng. 17 (2008) 567–575.
[7] M.I. Younis, F.M. Alsaleem, R. Miles, Q. Su, Characterization of the performance of capacitive switches activated by mechanical shock, J. Micromech. Microeng. 17 (2007) 1360–1370.
[8] D. Ciarlo, A latching accelerometer fabricated by the anisotropic etching of (1 1 0) oriented silicon wafers, J. Micromech. Microeng. 2 (1992) 10–13.
[9] M.R. Whitley, M. Kranz, R. Kesmodel, S. Burgett, Latching shock sensors for health monitoring and quality control, in: Proceedings of SPIE 5717, San Jose, CA, 2005, January 22, pp. 185–194.
[10] L.J. Currano, S. Bauman, W. Churaman, M. Peckerar, J. Wienke, S. Kim, M. Yu, B. Balachandran, Latching ultra-low power MEMS shock sensors for acceleration monitoring, Sens. Actuators A 147 (2008) 490–497.
[11] G.L. Smith, L. Fan, R.E. Balestrieri, D.L. Jean, Micromechanical Shock Sensor, U.S. Patent 6,737,979, 2004.
[12] S. Mariani, A. Ghisi, A. Corigliano, S. Zerbini, Multi-scale analysis of MEMS sensors subject to drop impacts, Sensors 7 (2007).
[13] M.J. Puttock, E.G. Thwaite, Elastic compression of spheres and cylinders at point and line contact, National Standards Laboratory Technical Paper No. 25, Commonwealth Scientific and Industrial Research Organization, Melbourne, Australia, 1969.
[14] L.J. Currano, D. Gee, M. Yu, B. Balachandran, Characterization of a no-power latching acceleration threshold sensor, in: Proceedings of 79th Shock and Vibration Symposium, October 26–30, Orlando, FL, 2008.
[15] L. Currano, M. Yu, B. Balachandran, Novel friction test structures for microelectormechanical systems, in: Proceedings of 2006 IMECE Paper 14054, November 5–10, Chicago, IL, 2006.